The Formation of Saturn's and Jupiter's Electron Radiation Belts by Magnetospheric Electric Fields

Yi-Xin Hao[1,2] , Yi-Xin Sun[1,2] , Elias Roussos[2,6] , Ying Liu[1] , Peter Kollmann[3] , Chong-Jing Yuan[4] , Norbert Krupp[2] , Chris Paranicas[3] , Xu-Zhi Zhou[1] , Go Murakami[5] , Hajime Kita[5] , and Qiu-Gang Zong[1]

[1] Institute of Space Physics and Applied Technology, Peking University, 100871, Beijing, People's Republic of China; qgzong@pku.edu.cn
[2] Max Planck Institute for Solar System Research, D-37077, Goettingen, Germany
[3] Johns Hopkins University Applied Physics Laboratory, Laurel, MD, USA
[4] Institute of Geology and Geophysics, Chinese Academy of Sciences, 100029, Beijing, People's Republic of China
[5] Institute of Space and Astronautical Science, Japan Aerospace Exploration Agency, Japan

Abstract

The existence of planetary radiation belts with relativistic electron components means that powerful acceleration mechanisms are operating within their volume. Mechanisms that bring charged particles planetward toward stronger magnetic fields can cause their heating. On the basis that electron fluxes in Saturn's radiation belts are enhanced over discrete energy intervals, previous studies have suggested that rapid inward plasma flows may be controlling the production of their most energetic electrons. However, rapid plasma inflows languish in the planet's inner magnetosphere, and they are not spatially appealing as a mechanism to form the belts. Here we show that slow, global-scale flows resulting from transient noon-to-midnight electric fields successfully explain the discretized flux spectra at quasi- and fully relativistic energies, and that they are ultimately responsible for the bulk of the highest energy electrons trapped at Saturn. This finding is surprising, given that plasma flows at Saturn are dominated by the planetary rotation; these weak electric field perturbations were previously considered impactful only over a very narrow electron energy range where the magnetic drifts of electrons cancel out with corotation. We also find quantitative evidence that ultrarelativistic electrons in Jupiter's radiation belts are accelerated by the same mechanism. Given that similar processes at Earth drive a less efficient electron transport compared to Saturn and Jupiter, the conclusion is emerging that global-scale electric fields can provide powerful relativistic electron acceleration, especially at strongly magnetized and fast-rotating astrophysical objects.

1. Introduction

Radiation belts are the toroidal regions in planetary magnetospheres that contain high fluxes of energetic charged particles. They form when planetary magnetic fields trap and accumulate energetic particles, produced through a variety of acceleration processes, at a rate that overcomes losses from energetic particle sinks. Because certain particle sinks, such as neutral-charged particle collisions or wave-particle scattering, could act over short timescales (e.g., days; Summers et al. 2007; Kollmann et al. 2011), adiabatic acceleration by slow radial diffusion alone (Roussos et al. 2007) may not always be sufficient to maintain the balance: rapid acceleration mechanisms are essential.

The requirement for a fast energetic particle source is particularly important for Saturn's electron radiation belt, which traps relativistic electrons up to several 10 MeV (Kollmann et al. 2011). This belt coexists with the planet's massive main ring system, an impenetrable obstacle that instantly absorbs trapped particle radiation coming in contact with them. While for other planets the equivalent terminal obstacle is their dense atmosphere (to which energetic particles reach after long trapping times in low-altitude, strong magnetic field regions), Saturn's main rings extend to an L-shell (L) of 2.27 and weaker magnetic fields, where particle residence is

shorter (L is the magnetic equatorial distance of a dipole field line, normalized to one Saturnian radius of 1 $R_S = 60{,}268$ km). Furthermore, Saturn's rotation-aligned dipole exposes trapped electrons continuously to an environment of large moons, Enceladus's E-ring and neutral gas cloud, and a variety of faint rings, all of which intensify losses, either through collisions or through scattering by electromagnetic ion cyclotron waves generated by the same environment (Kollmann et al. 2011; Meeks et al. 2016).

Several possibilities have been put forward to account for the missing, fast electron radiation belt source at Saturn, all with one or more caveats. Energy diffusion by whistler-mode chorus or Z-mode waves may be efficient inward of $L \approx 5$, but it cannot account for the high fluxes and energies of electrons farther out (Shprits et al. 2012; Woodfield et al. 2018, 2019). Contributions at $L \gtrsim 5$ may come from injections driven by a magnetospheric interchange instability (Chen & Hill 2008). However, because energetic electrons are observed to remain in the inflow channels of the injections for short periods, interchange-driven acceleration is typically efficient only up to ~50–100 keV (Paranicas et al. 2020), whereas the electron spectrum is observed to extend into the MeV range (Kollmann et al. 2011).

Electrons with energies that are much higher than 100 keV may be provided through a corotation drift resonance (CDR; Roussos et al. 2018): At energies around 1 MeV where the gradient and curvature drift of electrons cancels out

---

[6] Y. Hao, Y. Sun, and E. Roussos contributed equally to this work.

magnetospheric corotation (E_{CDR}; Thomsen & Van Allen 1980), convective electric fields that drive radial flows at fixed magnetospheric local times would dominate the electrons' motion, rapidly transporting and energizing them adiabatically across a large L-shell range. Observations of a noon-to-midnight electric field in Saturn's magnetosphere (or a radial inward flow at dusk; Thomsen et al. 2012; Wilson et al. 2013) and of a break in the electron spectrum tracking E_{CDR} for $4.5 < L < 8$ (Sun et al. 2019) suggest that CDR transport does indeed operate, at least for a narrow energy interval surrounding E_{CDR}. Whether or not convective transport and acceleration is important far from E_{CDR}, a possibility that has yet to be explored, is the main motivation behind the present investigation.

In this work, we use Cassini observations and simulations to establish that the effects of convection by Saturn's noon-to-midnight electric field extend well beyond E_{CDR} and dominate the dynamics of the bulk of Saturn's radiation belt electrons. In the context of these findings, we compare Van Allen Probes to Galileo and Juno energetic particle observations and assess the importance of convection-driven electron transport at the radiation belts of Earth and Jupiter.

2. Energy-banded Electron Spectra at Saturn ("Zebra Stripes")

2.1. Cassini Observations of "Zebra Stripes"

In Figures 1(A), (D) we show measurements of electron differential fluxes as a function of energy and L-shell that were obtained during crossings of the Cassini spacecraft through Saturn's radiation belts on two example days. The spectrograms feature a series of electron flux enhancements that are distributed across discrete energy intervals (bands). In Figures 1(B), (E) the appearance of the bands has been enhanced (see Appendix A), revealing that they span at least 6 R_S in radial extent and energies that reach above 1 MeV. All bands are dispersed such that their energy increases toward lower L-shells. We refer to these features as "zebra stripes" due to their resemblance with homonymous structures observed in the terrestrial inner radiation belt (Ukhorskiy et al. 2014; Liu et al. 2016).

The stripes are representative of a regular and dominant pattern in energetic electron spectra, recognized in many earlier works (Mitchell et al. 2015). It is often assumed that such dispersed patterns develop following the rapid injection of charged particles into the inner magnetosphere. This process populates a radial corridor with increased fluxes from where particles drift away with an energy, L-shell, and charge-dependent velocity (Thomsen & Van Allen 1980; Müller et al. 2010). However, known processes that may cause rapid planetward injections cannot explain the stripes' origin. The efficiency of magnetospheric interchange injections drops considerably above $\sim$100 keV, as already explained in Section 1. Injections following reconnection at Saturn's nightside magnetosphere may accelerate electrons closer to 1 MeV but only penetrate until $L \sim 10$ (Mitchell et al. 2015).

In Figures 1(C), (F) the energy has been converted into an azimuthal electron drift frequency (Appendix A). Stripes are evenly spaced and at quasi-constant drift frequencies. Such one-dimensional periodic structure in drift frequency has also been recognized in Earth's radiation belts (Liu et al. 2016) and originates from a superposition of an electric field in the magnetosphere that can drive radial electron transport. Because

a time-varying electric field with an approximate noon-to-midnight orientation has been measured throughout Saturn's inner and middle magnetosphere (Thomsen et al. 2012; Andriopoulou et al. 2013; Roussos et al. 2019), we tested if its presence can explain the zebra stripes.

2.2. Test Particle Simulations of Zebra Stripes

To explore the electric fields' impact on electron spectra we conducted a series of test-particle simulations where the trajectories of equatorially mirroring electrons were computed under the influence of Saturn's dipole field, corotation, and convection by a time-dependent, spatially uniform noon-to-midnight electric field. The electric field's amplitude is constrained by independent measurements (Thomsen et al. 2012; Andriopoulou et al. 2013; Wilson et al. 2013) and its variability is described as a sawtooth pulse, for reasons explained below and in Appendix B. Liouville's theorem, combined with mission-averaged electron spectra, are used to obtain the differential fluxes at the end of each simulation run (Appendix B). Within several tens of hours, energy-banded structures that resemble the Saturnian zebra stripes, both in energy and drift frequency space, had evolved from an initially smooth flux spectrogram (Figures 1(G), (H)). Similar results are obtained independently of our assumptions about the field's spatial distribution and temporal variations (Supplementary Figures 6, 7, Appendix B).

As the simulation evolved the number of zebra stripes was increasing (see Figure 9 in Appendix C and Supplementary Animation). Indeed, consecutive inbound and outbound passes of Cassini denote an increase in their number (Figure 2). Our model predicts that a few days after the sawtooth pulse the rising number of stripes would render them indistinguishable. Because stripe-free spectra at Saturn are not common (Paranicas et al. 2007, 2010; Müller et al. 2010), we deduce that enhancements in the electric field's intensity regenerate zebra stripes regularly, possibly over three weeks or shorter (a timescale based on Cassini's average orbital period).

To understand how zebra stripes form, we note that the noon-to-midnight electric field is equivalent to a plasma flow toward Saturn near dusk and away from it near dawn. These radial flow components break the local time symmetry of electron distributions by distorting the otherwise circular electron drift trajectories around Saturn. Even though these flows are slow ($<$3 km s^{-1} at $L \sim 5$), two effects amplify their impact: (a) their occurrence over global magnetospheric scales, and (b) Saturn's northward dipole leading to slower than corotation net azimuthal drifts of energetic electrons. Due to Saturn's fast rotation and strong magnetization, the strongest slowdown occurs for the highest energies studied here ($\sim$0.1–2 MeV, $4 < L < 10$). Within this energy range, this net azimuthal drift vanishes at the CDR energy (E_{CDR}) (Thomsen & Van Allen 1980; Roussos et al. 2018). The combination of these effects means that $\sim$0.1–2 MeV electrons are exposed to radial flows for long durations and experience large radial displacements. Following their radial transport, electrons of the same energy starting from different L-shells would disperse to form a spiral-like structure around the planet that increases its winding with time and crosses Cassini several times along its orbit (Müller et al. 2010). The timings of these crossings change for different electron energies, explaining why Cassini observes these electrons in the form of multiple, energy-dispersed stripes (Paranicas et al. 2007).
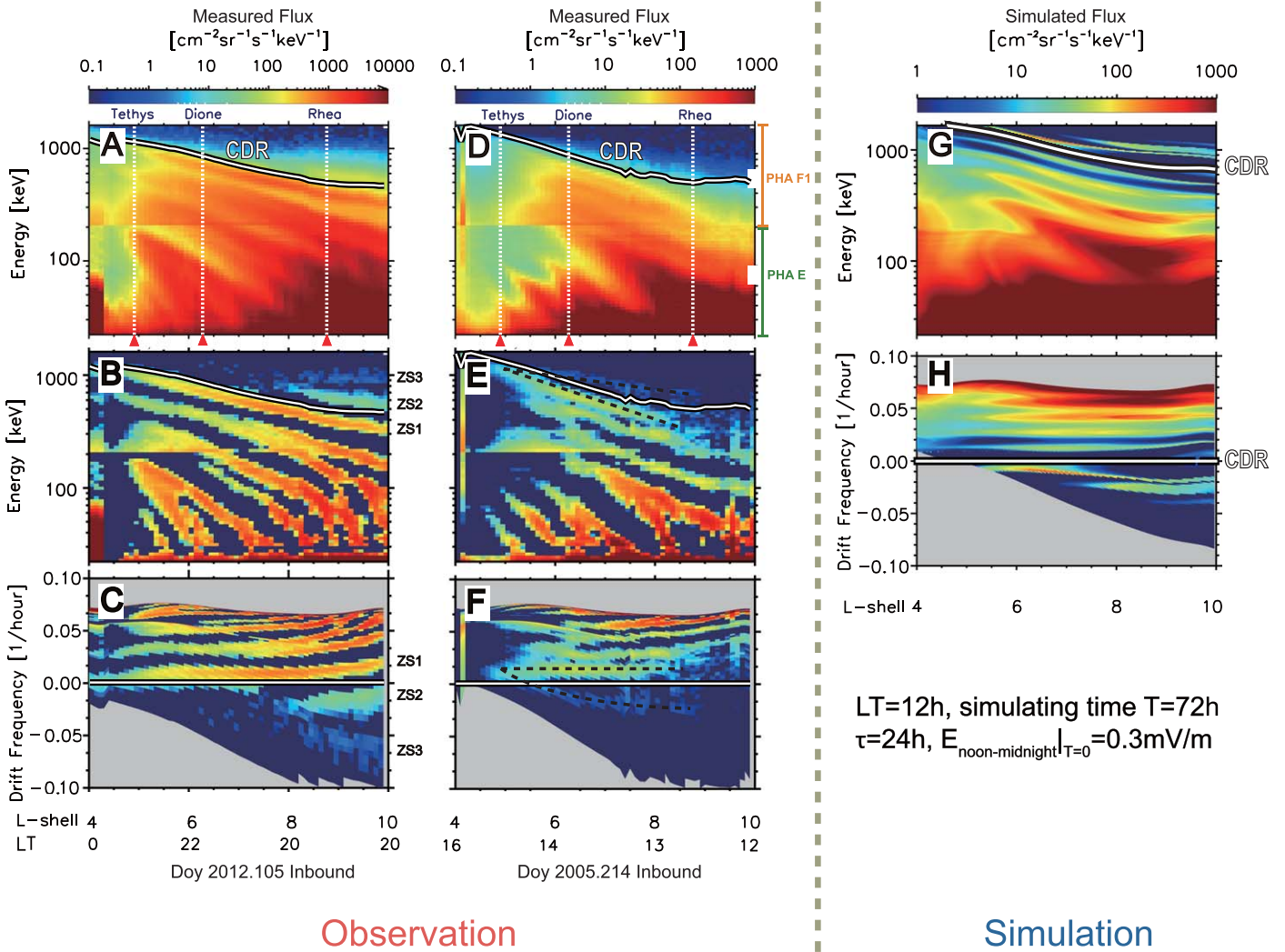
Figure 1. Zebra stripes in electron distributions from Saturn's radiation belts. (A), (C) Energetic electron spectrograms measured by the Low Energy Magnetospheric Measurement System (LEMMS) during two different orbits, processed spectrograms with the zebra stripes enhanced (B), (E) and their projection to drift frequency vs. L space (C), (F). A few of the zebra stripes that are discussed in the text are marked in panels (B), (C) as zs1–zs3. Similarly, a bifurcated stripe is marked in panels (E), (F) (dashed line). Some intersecting stripes with variable slopes below ~100 keV may come from interchange injections (Paranicas et al. 2016). Solid white lines indicate the energy where the drift frequency is zero (E_{CDR}). Vertical line segments mark the energies of the Pulse Height Analysis (PHA) channels of LEMMS, PHA-E and PHA-F1. The sharp spectral jump between them at ~200 keV is an instrumental artifact (Appendix A). Dotted lines indicate the L-shells of several of Saturn's major moons. Panels (G), (H) depict a simulated spectrogram from a test-particle model. The simulated spectrogram is a snapshot at $t = 72$ hr, as the number of stripes increases with time (see Figure 9 in Appendix C and Supplementary Animation).

Our simulations reconstruct several details of the stripes that can uniquely identify the noon-to-midnight electric field as their root cause. Around $E = E_{CDR}$, we predict that the stripes deviate from the constant drift frequency behavior and a single stripe can transition into a bifurcated one at $L > 6$ (Figures 1(G), (H)), a feature also observed with Cassini (Figures 1(E), (F), dashed lines). At energies near $E = E_{CDR}$ the electric field dominates the electrons' drift motion, forcing them to move on non-circumplanetary trajectories with a banana-shaped profile (Cooper et al. 1998; Roussos et al. 2019; Supplementary Figure 8). Each of the bifurcated stripe components contains electrons arriving to Cassini from distant L-shells, inward and outward with respect to its position. Furthermore, stripes near E_{CDR} are observed to be the most deeply penetrating ones (e.g., Figures 1(A), (B), stripe "zs1"), in agreement with our simulations. This occurs because for an

electric field with a fixed local time orientation, electrons are most efficiently moved in L-shell when they are close to E_{CDR} (Roussos et al. 2018). This energy dependence is particularly prominent for $E > E_{CDR}$, where both in our simulations and in the measurements stripes reach only down to $L \sim 6$ (Figures 1(B), (C) stripes zs2–zs3).

2.3. Impact of Electric Field–driven Transport of Energetic Electrons at Saturn

We can now use our model to quantify the radial electron transport and the associated adiabatic acceleration. In Figure 3 we show the output of such a simulation and the corresponding L-shell displacements experienced by electrons after exposure to a single electric field pulse. Electrons in the ~0.1–2.0 MeV range experience the largest displacements ($>1\,R_S$), and some may even
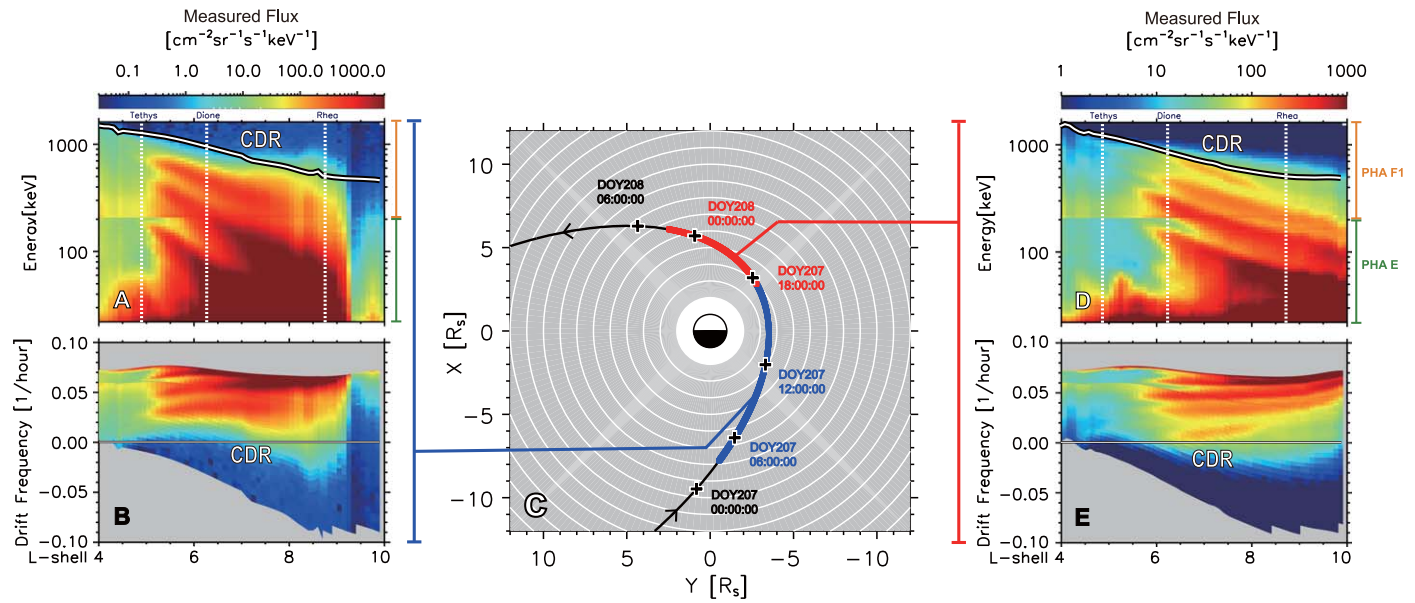
Figure 2. Continuous measurement of electron zebra stripes during an inbound–outbound orbit of Cassini. The left and right panels show an electron spectrogram measured by LEMMS during the inbound and outbound pass of Cassini on days 207–208/2009 and their projection to drift frequency-L space, respectively. The middle panel shows Cassini's orbit projected in the equatorial plane of Saturn, with $+x$ pointing toward noon and $+y$ toward dusk. Blue and red curves mark the inbound and outbound passes, respectively.
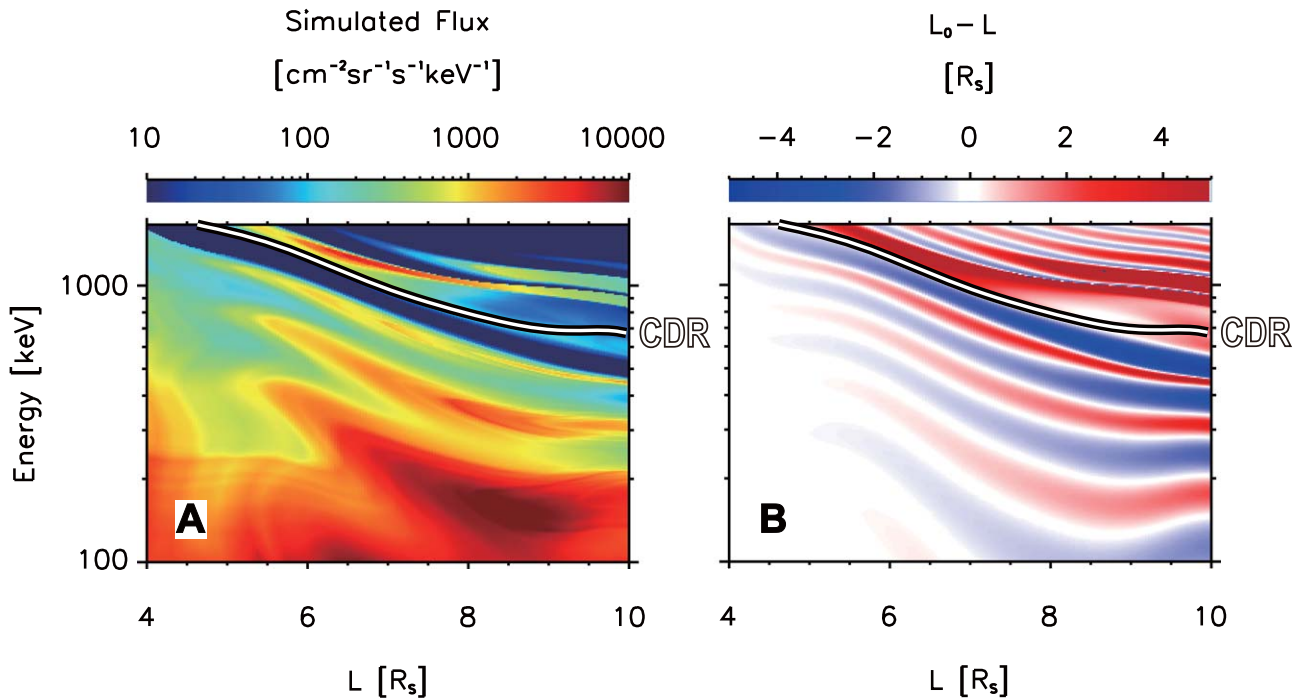

Figure 3. Left panel: simulated electron spectrograms as a function of L-shell and energy, similar to Figure 1(E) Right panel: the resulting L-shell displacement experienced by electrons from their initial position under the influence of a noon-to-midnight electric field pulse of 0.3 mV m^{-1} and after 72 hr of drift. The E_{CDR} energy is also marked as in Figure 1. Red stripes correspond to inward displacements, blue in outward displacements.

cross from the outer to the inner boundary of the plotted domain within a few days (red color, Figure 3), during which their energy increases about tenfold based on the assumed dipole field. Outward electron transport and cooling also takes place in parallel (blue color), but the net effect is that of an acceleration. This is because the phase space densities of >0.1 MeV electrons increase toward large distances (Kollmann et al. 2011), meaning that there

are more electrons available for inward transport than the other way around. Low-flux regions at $L < 7$ or $E > E_{CDR}$ become and remain populated (see Figure 9 in Appendix C and Supplementary Animation) under the action of the noon-to-midnight electric field, as the banded spectrograms indicate. The filling of the initially empty $E > E_{CDR}$ space, in particular, could be relevant to the regular observation of relativistic electron belt transients that carry
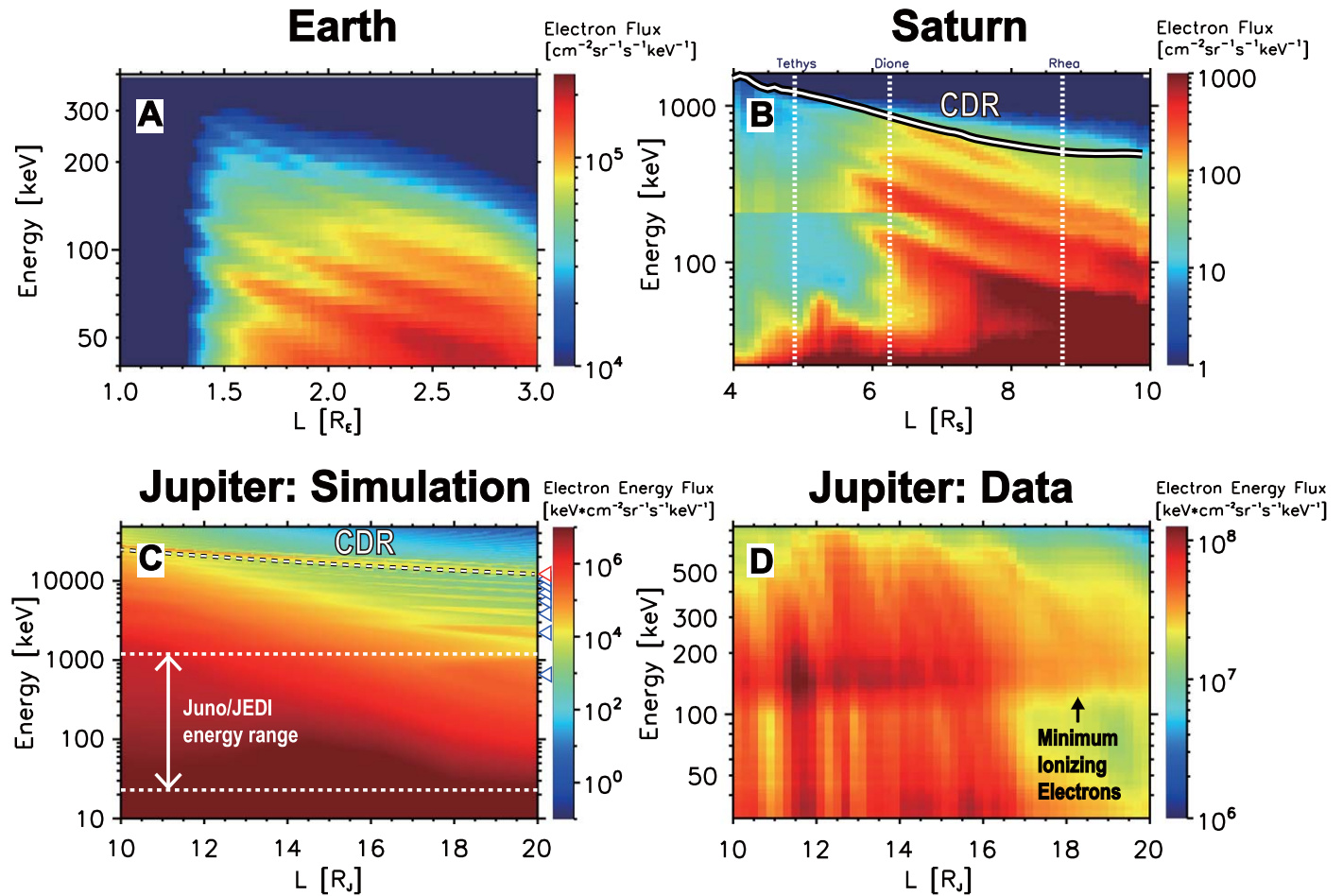
Figure 4. Comparison of energetic electron dynamics between Earth, Saturn, and Jupiter. (A) Zebra stripes observed in Earth's inner electron belt by the the Radiation Belt Storm Probes Ion Composition Experiment (RBSPICE) instrument on Van Allen Probe A. (B) Another example of zebra stripes observed in Saturn's radiation belt by Cassini (day 209/2007). (C) The topology of Jovian zebra stripes predicted by a test-particle model. The white dashed curve indicates E_{CDR}, triangles mark the center energy of zebra stripes at $L = 20.0$. The energy range of the Juno/Jupiter Energetic Particle Detector Instrument (JEDI) instrument is marked. Energy flux instead of differential flux is plotted to better contrast banded structures across a very large energy range (D) Jovian electron spectrogram measured by JEDI during Juno's PJ-8 inbound orbit. The horizontal band at ~150 keV is an instrumental artifact (Mauk et al. 2018).

high fluxes of MeV electrons at $L < 4$ (Yuan et al. 2020). Similar observations from Jupiter are discussed below.

3. Comparison between Saturn, Earth, and Jupiter

Earth's and Jupiter's radiation belts are also exposed to global-scale electric fields (Barbosa & Kivelson 1983; Burke 2007), but differences in the magnetospheric context greatly regulate their impact on electron dynamics. Earth's slow corotation and southward dipole orientation leads to relativistic electrons ($E \gtrsim 500$ keV) that drift around the planet in minutes in such a way that electric fields cannot easily move them radially (Selesnick et al. 2016). Electrons associated with the terrestrial zebra stripes (Figure 4(A)) are transported typically by a fraction of an Earth radius in the inner radiation belt ($L < 3$) (Sauvaud et al. 2013), an insignificant amount compared to what we find for Saturn. Short intervals of enhanced transport may partly fill the slot region that separates Earth's inner and outer electron radiation belts, but only up to ~900 keV and with an efficiency dropping exponentially with energy (Su et al. 2016; Turner et al. 2017). Subsequent losses in the slot region due to pitch-angle scattering rapidly limit planetward transmission and the production of relativistic electrons. As a result, the electron

spectrum of the inner radiation belt extends only up to ~1 MeV (Baker et al. 2014), while at Saturn it reaches beyond 10 MeV (Kollmann et al. 2011).

Jupiter is more similar to Saturn than to Earth: its northward dipole means that electrons drift slowly around E_{CDR}, which at Jupiter is above 10 MeV due to its even faster rotation and stronger magnetization compared to Saturn (Roussos et al. 2018). A dawn-to-dusk electric field observed in Jupiter's radiation belts (Barbosa & Kivelson 1983; Murakami et al. 2016) may lead to efficient electron transport and energization. Test-particle simulations conducted for the Jovian case as for Saturn indicate that the signature of this acceleration would also take the form of zebra stripes. Their characteristic energies, however, are well above ~1 MeV (Figure 4(C)), a range that has not been measured with high-energy resolution to date. Particularly, no stripes are predicted below ~1 MeV, an energy range monitored by the Jupiter Energetic Particle Detector Instrument (JEDI) on board the Juno spacecraft (Mauk et al. 2017), where mostly weakly energy-dispersed features are observed that are consistent with interchange injections (Figure 4(D)) (Haggerty et al. 2019).

Even though the predicted Jovian stripes could not be directly resolved, evidence for their presence may be deduced
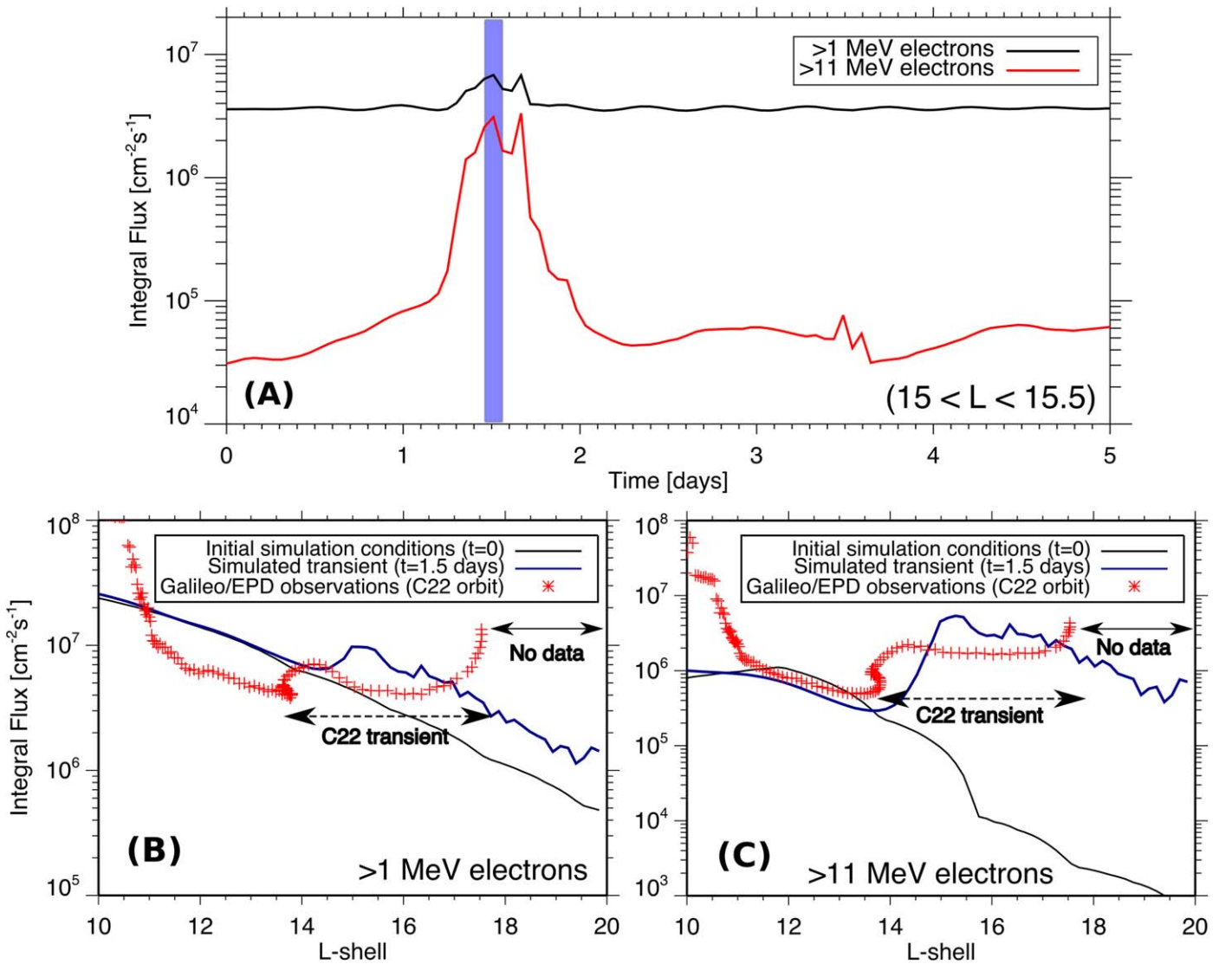
Figure 5. (A) Simulated time series of >11 MeV (red) and >1 MeV (black) integral electron fluxes at $15 < L < 15.5$ at Jupiter under the influence of a variable, dawn-to-dusk electric field (Murakami et al. 2016). Marked with a blue shaded area is the time step when simulated L-shell profiles are extracted for the two bottom panels (B), (C). Simulated L-shell profiles at $t = 1.5$ days into the simulation (dark blue), contrasted against the profiles at $t = 0$ red (initial simulation conditions, representing the average integral flux L-shell profiles based on Galileo observations), shown with a solid black curve. The integral fluxes for the inbound pass of Galileo during days 223–224/1999 (C22 orbit) are shown with red crosses and the location of the C22 transient is marked. The enhancement inward of $L = 11$ is within the envelope of the observed variations for that L-shell range (Jun et al. 2005), and its simulation is not considered here.

through the simulation of transient relativistic electron acceleration events that were measured by the Galileo spacecraft (Roussos et al. 2018). Their occurrence may be relevant to electron-flux enhancements near and above E_{CDR}, as already discussed for Saturn in Section 2.3. We thus repeated the test particle simulations of Figure 4(C), this time using measurements from the HISAKI Earth-orbiting telescope from a three-week period during which it observed several dawn-to-dusk electric field pulses (see Appendix A and Murakami et al. 2016), and explore if electron belt transients follow episodic changes in the electric field's amplitude.

In order to compare the model with the available observations that only provide integral fluxes, the simulated electron spectra were converted into time series and L-shell distributions of integral flux at >1 MeV and >11 MeV (Figure 5). On the second day of the simulation, a strong enhancement occurs for >11 MeV electrons, the fluxes of which receive large contributions from electrons near E_{CDR}. Fluxes of >1 MeV

electrons, dominated by non-resonant particles (Figure 5(A)), experience a milder enhancement. The relative enhancement between these two energy ranges is a key signature of the best resolved transient recorded by the Galileo spacecraft (days 223–224/1999, orbit C22; Roussos et al. 2018). Similarly, trends in the L-shell profile of the C22 transient are also approximated: the simulated enhancement's amplitude increases toward larger L-shells, as observed in Figure 5(B), (C). Therefore, we may deduce that banded spectra with a strong E_{CDR} flux peak, signifying efficient electric field-driven transport, develop also at Jupiter for ultrarelativistic electrons.

4. Summary and Conclusions

We have demonstrated that adiabatic electron acceleration by global-scale electric fields is a particularly efficient process at Saturn and Jupiter due to the planets' stronger magnetization, opposite magnetic field orientation, and faster corotation relative to Earth's. At Saturn, this process leaves clear

signatures in the data in the form of zebra stripes that dominate electron spectra at $L > 4$ and ~ 0.1–2 MeV. This finding demonstrates that convection impacts a very broad spectrum of electrons, while earlier studies (Kollmann et al. 2018; Roussos et al. 2018; Sun et al. 2019) suggested that this would only be the case for energies that are very close to E_{CDR}. Competing acceleration processes by interchange or wave-particle interactions cannot explain the zebra stripe observations shown here. The extension of the noon-to-midnight electric field down to Saturn's main rings ($L \sim 2.27$) suggests that this acceleration mode remains important also in the innermost belts (Roussos et al. 2019; Yuan et al. 2020), but experimental limitations currently prevent us from resolving electron spectra with high-energy resolution for $L < 4$. At Jupiter, quantitative evidence that is consistent with electron convection is found in the properties of transients that are potentially delivering high fluxes of ultrarelativistic electrons closer to the planet and power its synchrotron-emitting radiation belts. The fact that the latter appear to be regulated by dawn-to-dusk electric field dynamics (Han et al. 2018) supports this link. Electric field–driven acceleration is therefore a fundamental acceleration process for planetary radiation belts with a major, if not dominant, role at Saturn, Jupiter, and possibly at other strongly magnetized and fast-rotating astrophysical objects such as ultracool brown dwarfs (Williams 2018).

Appendix A
Information on Datasets and Their Processing

A.1. Cassini

Energetic electron measurements at Saturn are from LEMMS on board the Cassini satellite. LEMMS was a double-sided particle telescope that belonged to the Magnetosphere Imaging Instrument (MIMI) package (Krimigis et al. 2004). Here we use two sets of LEMMS's PHA electron channels, namely PHA-E and PHA-F1, which belong to its Low Energy Telescope. They measure electrons from 20 keV to 2.3 MeV with a high energy resolution (two sets of 64 logarithmically spaced energy bins). Measurements up to ~ 1.6 MeV are shown here, particularly because channel efficiency drops substantially above that. PHA-E and PHA-F1 overlap at 140–420 keV. We select fluxes below 200 keV from the PHA-E channels and above 200 keV from the F1 channels. Fluxes at this overlapping energy range

may disagree due to contamination by penetrating MeV electrons in the radiation belts or low counting statistics, but this does not impact our conclusions, as we primarily focus on stripe profiles and less on their flux content. In order to highlight the stripe profiles (Figures 1(B), (E)), we subtract a background PHA spectrogram from the actual one, after PHA-E and F1 have been combined. This background spectrogram is obtained by a nine-point smoothing in both energy and L-shell to the data of the respective orbit. Analysis of the PHA channels was restricted outside $L = 4$. Inward of that distance, the contamination by high fluxes of MeV electrons and protons cannot be corrected. Magnetic field measurements provided by the Magnometer (MAG) instrument (Dougherty et al. 2004) are used to determine particle pitch angles and the E_{CDR} energy (Sun et al. 2019).

A.2. Juno

Juno energetic electron data (Figure 4(D)) are from the JEDI instrument (Mauk et al. 2013) and the inbound portion of the mission's perijove 8 (PJ8: 2017 September 1/14:30–19:30 UTC; Haggerty et al. 2019). JEDI measures electrons in the energy range from 30 keV to about 1 MeV. The instrument comprises three sensors, each having six look directions. The spectrogram of Figure 5(D) is an average from all JEDI sensors and look directions at that time period. A horizontal band at about 100 keV is an artifact from minimum ionizing, penetrating MeV electrons (Mauk et al. 2018). L-shell values are based on the VIP4 internal field model and the CAN current sheet model (Connerney et al. 1981). Precalculated values were obtained from http://lasp.colorado.edu/home/mop/missions/juno/trajectory-information/, specifically http://lasp.colorado.edu/home/mop/files/2018/02/juno2018Jan22_Reduced08.sav_.zip ("CANsheet" model). We note that the Juno project uses the terminology "M-shell" to indicate that this mapping is performed using a Jovian magnetic field model other than a dipole. For consistency, we use "L-shell" throughout the manuscript.

A.3. Galileo

Galileo energetic particle data shown in Figures 5(B), (C) are from the Energetic Particle Detector (EPD). EPD comprised several detectors, from which we use EPD/LEMMS that could measure electrons from 15 keV up to the tens of MeV range. The measurements shown in Figures 5(B), (C) are from integral energy channels DC2 and DC3, measuring approximately electrons of >1 MeV and >11 MeV, respectively. Measurements by EPD/LEMMS are available both as differential energy flux spectra obtained through spectral inversions (Kollmann et al. 2018), and as raw integral fluxes, obtained by dividing the channel count rates by their average geometry factor. Measurements shown in 5(B), (C) for the C22 event are raw integral fluxes. The processed measurements and user guide for EPD can be obtained from http://sd-www.jhuapl.edu/Galileo_EPD/.

A.4. HISAKI

Dawn-to-dusk electric field estimations at Jupiter are based on observations by the HISAKI Earth-orbiting telescope (Yoshioka et al. 2013; Yamazaki et al. 2014; Yoshikawa et al. 2014) in the ultraviolet (UV) wavelength range. HISAKI has been monitoring Jupiter since 2013. The electric field is estimated through the observation of UV brightness

asymmetries between the dawn and dusk segments of the Io torus at $L = 5.9$. The time series used for the simulation shown in Figure 5(E), are from 2013 December 21 to 2014 January 10 (Murakami et al. 2016). We used this time period in order to represent a realistic spectrum of the variations that the dawn-to-dusk electric field may experience over extended time intervals and to explore the feasibility that these can give rise to radiation belt transients. For the simulations shown in Figure 5, the magnitude of the electric field was reduced by a factor of five, for reasons explained in the simulations subsection. No simultaneous estimations of the dawn-to-dusk electric field are available for the date of the C22 event that we refer to in Figure 5(E), which was observed by Galileo in 1999 (Roussos et al. 2018).

A.5. Van Allen Probes

Earth radiation belt measurements in Figure 4(A) are from RBSPICE that operated in orbit around Earth between 2012 and 2020. RBSPICE has six telescopes detecting electrons in the energy range from 25 keV to 1 MeV with 64 logarith- mically spaced energy bins (Mitchell et al. 2013). The spectrogram shown displays directionally averaged data.

A.6. Processing of MIMI/LEMMS Measured and Simulated Spectrograms

To convert the electron energy to bounced-averaged drift frequency around Saturn (e.g., Figures 1(B), (D)), plasma corotation and magnetic drifts are taken into account as follows:

$$f_{\text{drift}} = \frac{\Omega_{\text{corot}}(L)}{2\pi} - \frac{3\gamma m_0 \beta^2 c^2}{4\pi e B_S R_S^2} L(0.7 + 0.3\sin\alpha_{\text{eq}}). \quad \text{(A1)}$$

We adapted an L-dependent (sub)corotation profile ($\Omega_{\text{corot}}(L)$) that is based on plasma ion velocity measurements (Wilson et al. 2009). The magnetic gradient and curvature drift frequency is calculated from the second term of Equation (A1), where m_0 is the rest mass, c is the speed of light, β is the ratio of v to c, γ is the relativistic Lorentz factor, B_S is the equatorial surface magnetic field at Saturn (0.21 G), R_S is the radius of Saturn (1 $R_S = 60{,}268$ km) and α_{eq} is the electrons' equatorial pitch angle. The equation is readily applicable for Jupiter, by adjusting the values for the corotation (we approximate it with rigid), surface magnetic field (4.17 G) (Connerney et al. 2018), and planetary radius (1 $R_J = 71{,}492$ km). The use of the dipole approximation is sufficient for the purpose of our study. The CDR energy can be obtained from solving $f_{\text{drift}} = 0$.

Appendix B
Test Particle Model

The synthetic spectra and the flux spectrograms generated for evaluating electron transport and acceleration by convective electric fields are evaluated in three steps. The first step requires predefining the electric and magnetic field models under which the tracing will be performed. The second involves the evaluation of energetic electron trajectories, and the third involves the derivation of electron fluxes at a desired location and time through a flux normalization process. These steps are described below. We note that for all calculations, a cylindrical coordinate system with its z-axis aligned with Saturn's or Jupiter's dipole axis is used.

B.1. Electric and Magnetic Field Models

For both Saturn and Jupiter, the magnetic field model and corotation were treated as mentioned earlier in the sections about converting electron energy to drift frequency. For the noon-to-midnight electric field of Saturn (Andriopoulou et al. 2013) and the dawn-to-dusk electric field of Jupiter (Barbosa & Kivelson 1983), we assumed that they are time-variable and spatially uniform. Excluding Figure 5, the time variability was introduced in the form of a sawtooth pulse. In the case of Saturn, the electric field has the form:

$$\boldsymbol{E}_{\text{noon-midnight}}(t)$$
$$= \begin{cases} -E_0 e^{-t/\tau}\sin\phi\boldsymbol{e}_r - E_0 e^{-t/\tau}\cos\phi\boldsymbol{e}_\phi & t \geqslant 0; \\ 0 & t < 0, \end{cases} \quad \text{(B1)}$$

where the noon-to-midnight electric field amplitude is $E_0 = 0.3\,\text{mV m}^{-1}$, ϕ controls the magnetospheric local time and $\tau = 24$ hr is the e-folding time of the damping electric field. The amplitude of the electric field is based on measured values (Thomsen et al. 2012; Andriopoulou et al. 2013; Wilson et al. 2013). The damping time is less constrained, but its exact value had no impact on the appearance of the stripes.

To evaluate how our choice for τ did not impact the appearance of energy-banded spectra, the opposite extreme was also simulated, i.e., a constant electric field. This corresponds to an infinite value for τ (or $e^{-t/\tau} = 1$), thus encompassing a broad range of possibilities for the pulse's decay and shape. Supplementary Figure 6 shows that stripes also appear in this case. A caveat of a constant electric field is that it also leads to continuous, strong outward electron transport, with many electrons reaching the large distances and/or the magneto- pause, particularly at $E = E_{\text{CDR}}$. Small values of τ (e.g., less than few hours) have been excluded because the reconstruction of the topology of energetic electron moon wakes (Roussos et al. 2013), which is controlled by the noon-to-midnight electric field, requires the electric field to be persistent for at least 6–8 hr.

As several studies indicate that the electric field at Saturn drops with L-shell (Thomsen et al. 2012; Andriopoulou et al. 2013; Wilson et al. 2013), we have also used a Volland–Stern type model for the electric field (Burke 2007) that scales the electric field as

$$\boldsymbol{E}_{\text{noon-midnight(VS)}}(t)$$
$$= \begin{cases} -E_0 e^{-t/\tau}(L/L_0)^{\overline{\gamma}-1}(\overline{\gamma}\sin\phi\boldsymbol{e}_r + \cos\phi\boldsymbol{e}_\phi) & t \geqslant 0; \\ 0 & t < 0. \end{cases} \quad \text{(B2)}$$

Here, E_0 is the electric field value at ($t = 0$, $L_0 = 5$, $LT = 6$ hr) while $\overline{\gamma}$ is a unitless index controlling the electric field's spatial variation. For $\overline{\gamma} = 1$ we revert to the uniform electric field case. For $\overline{\gamma} < 1$, the electric field decreases with L for a given local time (ϕ). On the other hand, the magnitude of $\boldsymbol{E}_{\text{noon-midnight(VS)}}$ becomes dependent on ϕ (local time) for a fixed L-shell, a characteristic that we cannot constrain from existing electric field estimations. With that in mind, we used $\overline{\gamma} = 0.5$ to approximate the observed dropout of the electric field with L, while restricting the ϕ-dependent amplitude variations to a very small range. Supplementary Figure 7 shows that even with such a spatially varying electric field there is no impact on the appearance of the striped spectra.
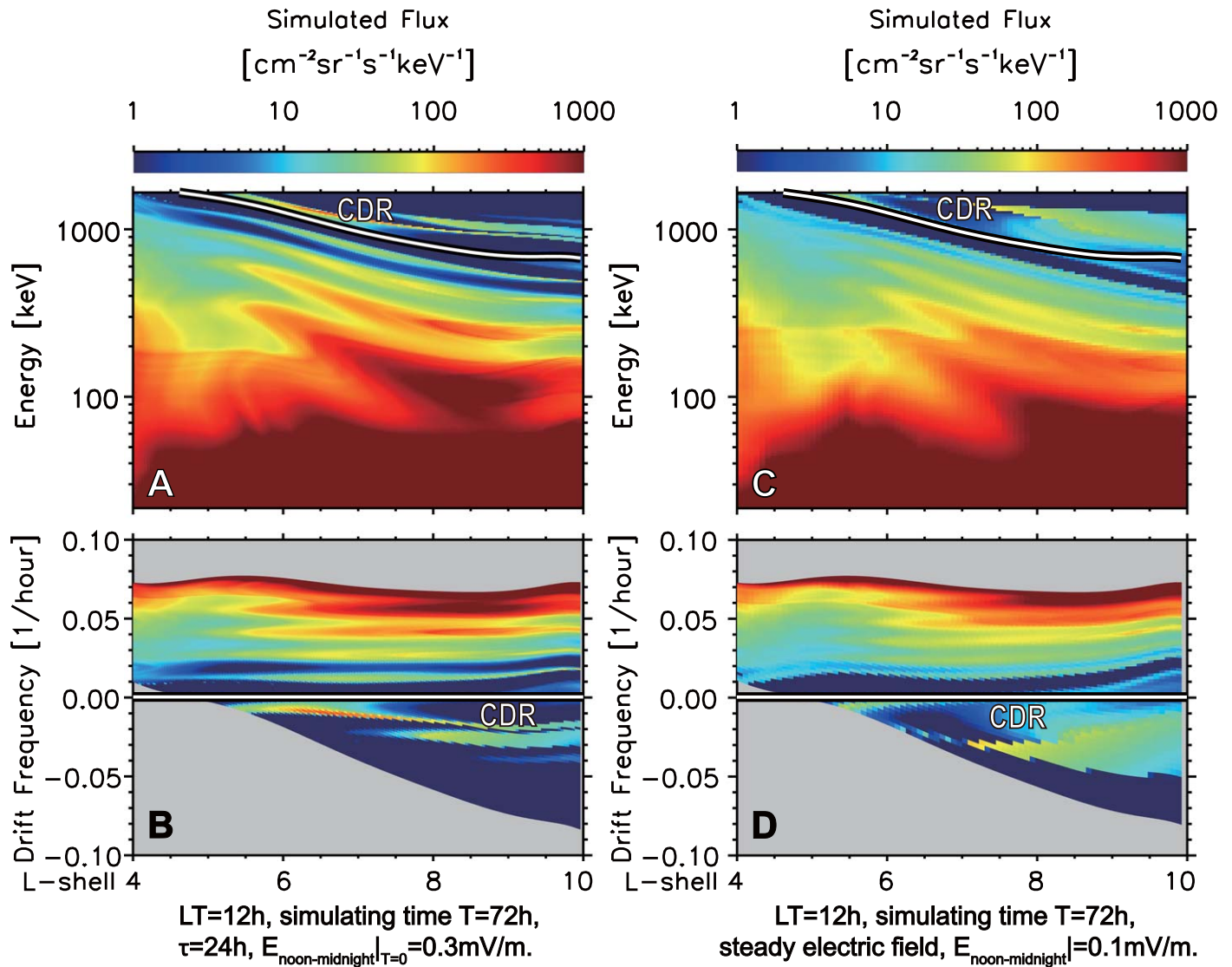
Figure 6. Comparison between the evolution of the electron distributions driven by noon-to-midnight electric field in the form of a sawtooth pulse (left panels) or with constant amplitude (right panels). Panels are in the same format with Figures 1(G), (H). The change in the electric field properties modify the number of stripes, their spacing and flux content for a given simulation time step; however, zebra-stripes, looking similar to the observations, still emerge.

Based on the findings described above, a uniform electric field was finally chosen as the baseline, because the observed radial drop-off of the noon-to-midnight electric field is small within the simulated L-shell range and represents an average condition that was not always resolved in individual Cassini orbits (Andriopoulou et al. 2013).

For Jupiter, Equation (2) was adjusted for an electric field with a dawn-to-dusk orientation. The electric field's magnitude and variations at Jupiter are constrained through observations by the HISAKI telescope (Murakami et al. 2016), albeit only near Io's orbit ($L \sim 5.9$). The scaling of the electric field with distance is not constrained. For this reason, a uniform dawn-to-dusk electric field was used throughout, as in earlier studies (Han et al. 2018). The magnitude of the electric field was chosen in a way to explore its feasibility to drive efficient acceleration. A sawtooth profile peaking at 3.0 mV m^{-1} and with a temporal damping of $\tau = 24$ hr was considered for generating the results of Figure 4(C). For the results shown in

Figure 5(E), the sawtooth pulse model was replaced by observed variations of the electric field (Murakami et al. 2016). The amplitude of the electric field time series, however, was reduced by a factor of five to ensure stability of our tracings over a simulated period of three weeks when electrons are constantly exposed to radial flows. A constantly present electric field with an intensity like that inferred for Io's distance causes strong outward transport of electrons near E_{CDR} and losses of many test particles from the simulation domain when these reach large distances, as also discussed for Saturn. As key aspects of the C22 transient were reconstructed, we deduce that at $L > 10$ convection-driven acceleration remains very efficient even with electric field amplitudes that are much weaker than at Io ($L = 5.9$). The reduced electric field magnitude used is not unrealistic for the L-shell range simulated. Flows between 10 and 30 km s^{-1} would have been expected beyond $L = 10$ around noon or midnight if the electric field was as strong as inferred for Io's distance. Radial flow estimates inward of
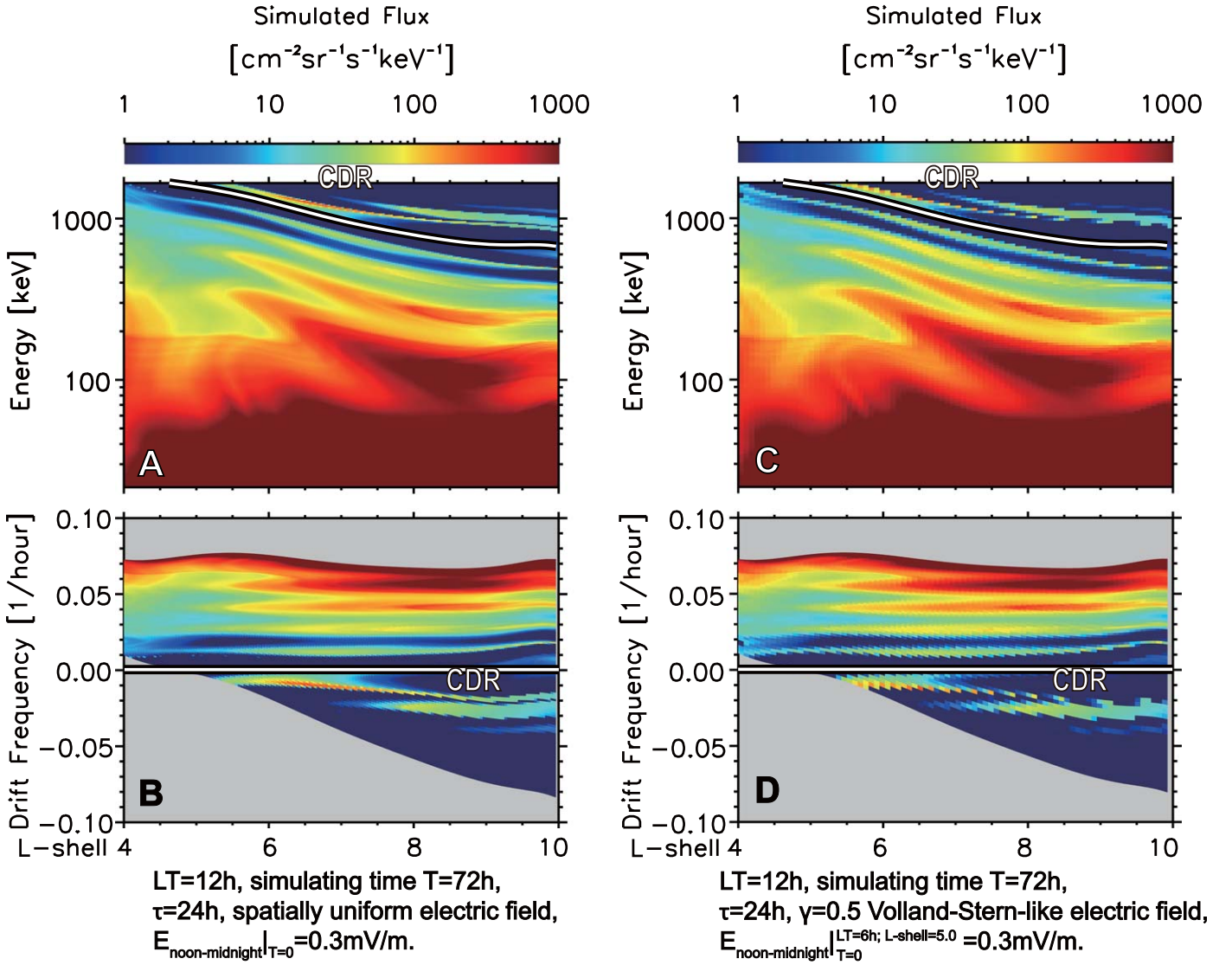
Figure 7. Comparison between the evolution of the electron distributions driven by a uniform noon-to-midnight electric field in the form of a sawtooth pulse (left panels) or with noon-to-midnight electric field with an amplitude dropping with L-shell (right panels). The profile of the spatially varying electric field follows a Volland–Stern model. Panels are in the same format with 1(G), (H). Negligible changes are only visible between the two simulation outputs.

$L \sim 15$, where they are most reliably resolved, do not favor velocities above $10 \, \mathrm{km \, s^{-1}}$ (Bagenal et al. 2016).

B.2. Simulating the Trajectory of Electrons

With a model for the electric field established, the motion of equatorial mirroring electrons was obtained by Liu et al. (2016)

$$\begin{cases} \dot{L} = \frac{E_\phi}{R_S B_S} L^3; \\ \dot{\phi} = \Omega_{\mathrm{corot}}(L) - \frac{3\gamma m_0 \beta^2 c^2}{2 e B_S R_S^2} L - \frac{E_r}{B_S R_S} L^2, \end{cases} \quad \text{(B3)}$$

where $(\dot{L}, \dot{\phi})$ is the time derivative of spatial coordinates (L, ϕ) and E_r (E_ϕ) is the radial (azimuthal) component of $\boldsymbol{E}_{\mathrm{noon-midnight}}(t)$. The first adiabatic invariant $\mu = p_\perp^2/(2m_0 B)$ of each particle is conserved at each time step, where $p_\perp$ is the perpendicular momentum of the particle and $B = B_S/L^3$ is the dipole magnetic field strength at the particle's L-shell. This is a valid assumption given that the timescales associated with the first invariant are orders of magnitude shorter compared to the

electric field variations described. For the equatorial particles, it is $p = p_\perp$. A fourth-order Runge–Kutta method was sufficient to integrate the equations of motion. Electron trajectories at Jupiter were calculated in the same way, with values in Equation (3) adapted for the Jovian case, as discussed in the context of Equation (1).

B.3. Simulating the Radiation Belt Evolution

Electrons are defined initially as test particles for $4 < L < 10$ and 0.02–2 MeV and for a selected magnetospheric local time (longitude), and their position is tracked for a duration and a time resolution based on the purpose of each simulation run. We note that the longitude corresponds to that of the virtual detector, and does not represent a preferential location that particles are injected, as explained below.

In order to model the electron flux profile $j(E_k, L)$ at a given time t and longitude ϕ, electrons with each value of (E_k, L) were traced backward in time along the calculated trajectories to determine their initial position (L_0, ϕ_0) at t_0, i.e., from which
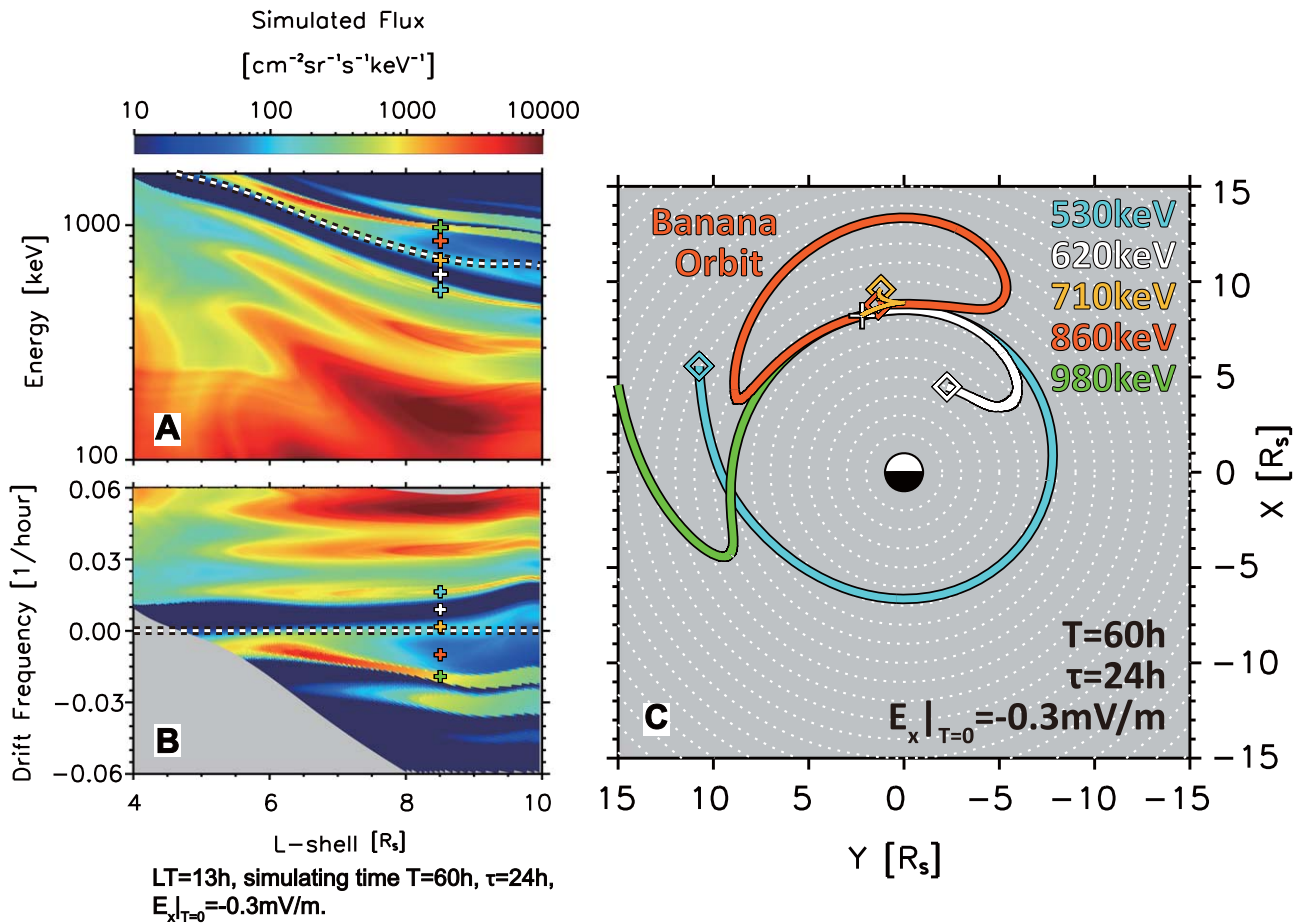
Figure 8. Left panels (A), (B): simulated electron spectrogram as a function of *L*-shell and energy at the top or *L*-shell and drift frequency at the bottom. Crosses of different colors mark individual energies, some of which are along a bifurcated zebra stripe. Representative electron trajectories from that energy range are indicated in the right panel (C) with the same colors. The trajectories indicate the initial position of the respective electrons and what path they followed the 60 hr before their detection at the point marked with a white cross. In this projection, the *xy*-plane corresponds to Saturn's equatorial plane, with +*x* pointing toward the Sun and +*y* toward dusk. The bifurcated stripe occurs in the energy range where electrons, under the action of the noon-to-midnight electric field, do not move on circumplanetary trajectories, but on paths with a banana-shaped profile.

location particles reach the virtual detector. According to Liouville's theorem, the phase space density $f(\mu, L, \phi, t)$ should equal the initial value $f(\mu_0, L_0, \phi_0, t_0)$, where the first adiabatic invariant μ of each particle is conserved ($\mu = \mu_0$), implying that E_k changes with L. Therefore, the flux j at each (E_k, L) can be determined by the phase space density value at the initial position of each particle, assuming no sources or losses act along the trajectories. The conversion between flux and phase space density follows $j = p^2 f$. If particles arrive from outside the magnetopause or inward of Saturn's main ring edge ($L < 2.27$), then $j = 0$.

A mission-averaged electron differential flux as a function of energy and *L*-shell from LEMMS measurements was adapted as the initial distribution $j(E_k, L)$ to model the evolution of Saturnian radiation belt. The averages were obtained by applying a median filter on measurements with $\alpha_{eq} > 10°$. To provide an initially smooth distribution, fluxes of the PHA-E channels were changed artificially to match those from the PHA-F1 channels at their overlapping energy range. When modeling the Jovian radiation belt, the differential flux model was based on spectra available through inversions of Galileo/EPD measurements by Kollmann et al. (2018). The inversions are available as time series of three spectral coefficients, which we have spatially binned in order to obtain the average Jovian

energetic electron spectra as a function of *L*-shell. The spectra by Kollmann et al. (2018) were preferred over those from the Galileo Interim Electron Environment (GIRE) model (Garrett et al. 2012) that constrains fluxes only up to ~40 R_J.

For each of the simulations, the longitude (local time) of the virtual detector was kept constant and was set to $LT = 12$ hr for Figures 1–4. This choice has no impact on our results or the emergence of the stripes, besides the appearance of the bifurcated stripe at E_{CDR}, which for a noon-to-midnight electric field it preferentially occurs at dayside local times (Figure 1, Supplementary Figure 8). For the simulations of Figure 5, $LT = 4$ hr as C22 event was observed in the pre-dawn sector. Because Cassini's or Galileo's velocity components in both *L*-shell and azimuth are non-zero the detection sequence of stripes at high energies may be affected. This effect is particularly important if we want to reconstruct the exact timing of stripes. As our simulations focus on the origin of the stripes, neglecting the spacecraft velocity is not critical.

Appendix C
Additional Supporting Figures

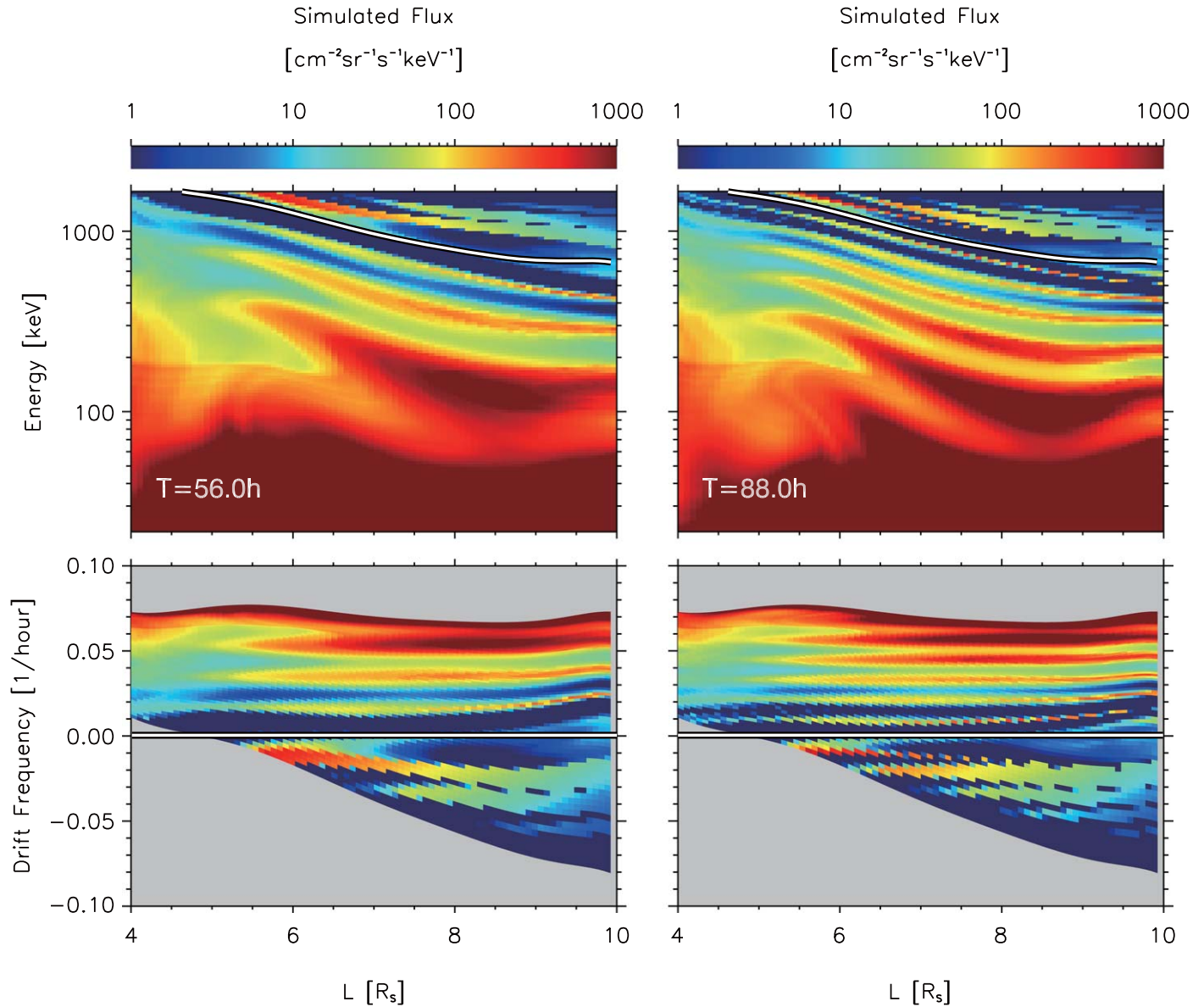This Appendix includes Supplementary Figures 8 and 9.

Figure 9. Temporal evolution of the simulated energetic electron fluxes as a function of L-shell and kinetic energy (top two panels) or as a function of L-shell and electron drift frequency (bottom two panels). The corresponding spectrograms evolve from an initially smooth flux distribution that at $t = 0$ we exposed to a sawtooth noon-to-midnight electric field pulse with a peak amplitude of $E_o = 0.3$ mV m^{-1} and a damping time of $\tau = 24$ hr. The left and right plot panels are snapshots of the spectrogram evolution at $t = 56$ hr and $t = 88$ hr, respectively, showing the appearance of the zebra-stripe patterns and the increase of the stripe number with increasing time, as described in Section 2.2. The thick white line in each panel corresponds to the energy of the corotation drift resonance (top row), or to the equivalent zero drift frequency regime (bottom row). An animated version of the figure is provided, where the formation and gradual increase in stripe number is visualized between $t = 0$ and $t = 99$ hr (animation duration: 4 s). The development and increase in stripe number is best visible above 100 keV or for drift frequencies lower than 0.06 deg hr^{-1}.

(An animation of this figure is available.)

ORCID iDs

Yi-Xin Hao https://orcid.org/0000-0003-0425-3358
Yi-Xin Sun https://orcid.org/0000-0003-3568-4839
Elias Roussos https://orcid.org/0000-0002-5699-0678
Ying Liu https://orcid.org/0000-0002-1674-849X
Peter Kollmann https://orcid.org/0000-0002-4274-9760
Chong-Jing Yuan https://orcid.org/0000-0003-1434-5803
Norbert Krupp https://orcid.org/0000-0003-4683-9533
Chris Paranicas https://orcid.org/0000-0002-4391-8255
Xu-Zhi Zhou https://orcid.org/0000-0003-4953-1761
Go Murakami https://orcid.org/0000-0001-9269-5855
Hajime Kita https://orcid.org/0000-0001-9948-5316
Qiu-Gang Zong https://orcid.org/0000-0002-6414-3794

References

Andriopoulou, M., Roussos, E., Krupp, N., et al. 2013, Icar, 229, 57
Bagenal, F., Wilson, R. J., Siler, S., Paterson, W. R., & Kurth, W. S. 2016, JGRE, 121, 871
Baker, D. N., Jaynes, A. N., Hoxie, V. C., et al. 2014, Natur, 515, 531
Barbosa, D. D., & Kivelson, M. G. 1983, GeoRL, 10, 210
Burke, W. J. 2007, JASTP, 69, 1114
Chen, Y., & Hill, T. W. 2008, JGRA, 113, A07215
Connerney, J. E. P., Acuna, M. H., & Ness, N. F. 1981, JGR, 86, 8370
Connerney, J. E. P., Kotsiaros, S., Oliversen, R. J., et al. 2018, GeoRL, 45, 2590
Cooper, J. F., Sittler, E. C., Maurice, S., Mauk, B. H., & Selesnick, R. S. 1998, AdSpR, 21, 1479
Dougherty, M. K., Kellock, S., Southwood, D. J., et al. 2004, SSRv, 114, 331

Garrett, H., Kokorowski, M., Jun, I., & Evans, R. 2012, Galileo Interim Radiation Electron Model: Update 2012, Tech. Rep. 12-9, 2012, Pasadena, CAJet Propulsion Laboratory, National Aeronautics and Space, https://trs.jpl.nasa.gov/handle/2014/42026?show=full

Haggerty, D. K., Mauk, B. H., Paranicas, C. P., et al. 2019, GeoRL, 46, 9397

Han, S., Murakami, G., Kita, H., et al. 2018, JGRA, 123, 9508

Jun, I., Garrett, H. B., Swimm, R., Evans, R. W., & Clough, G. 2005, Icar, 178, 386

Kollmann, P., Roussos, E., Paranicas, C., et al. 2011, JGRA, 116, A05222

Kollmann, P., Roussos, E., Paranicas, C. P., et al. 2018, JGRA, 123, 9110

Krimigis, S. M., Mitchell, D. G., Hamilton, D. C., et al. 2004, SSRv, 114, 233

Liu, Y., Zong, Q. G., Zhou, X. Z., Foster, J. C., & Rankin, R. 2016, JGRA, 121, 4145

Mauk, B., Haggerty, D., Jaskulek, S., et al. 2017, SSRv, 213, 289

Mauk, B. H., Fox, N. J., Kanekal, S. G., et al. 2013, SSRv, 179, 3

Mauk, B. H., Haggerty, D. K., Paranicas, C., et al. 2018, GeoRL, 45, 1277

Meeks, Z., Simon, S., & Kabanovic, S. 2016, P&SS, 129, 47

Mitchell, D. G., Brandt, P. C., Carbary, J. F., et al. 2015, Injection, Interchange, and Reconnection (New York: Wiley), 327

Mitchell, D. G., Lanzerotti, L. J., Kim, C. K., et al. 2013, SSRv, 179, 263

Müller, A. L., Saur, J., Krupp, N., et al. 2010, JGRA, 115, A08203

Murakami, G., Yoshioka, K., Yamazaki, A., et al. 2016, GeoRL, 43, 12308

Paranicas, C., Mitchell, D. G., Roelof, E. C., et al. 2007, GeoRL, 34, 2109

Paranicas, C., Mitchell, D. G., Roussos, E., et al. 2010, JGRA, 115, 9214

Paranicas, C., Thomsen, M. F., Achilleos, N., et al. 2016, Icar, 264, 342

Paranicas, C., Thomsen, M. F., Kollmann, P., et al. 2020, JGRA, 125, e28299

Roussos, E., Andriopoulou, M., Krupp, N., et al. 2013, Icar, 226, 1595

Roussos, E., Jones, G. H., Krupp, N., et al. 2007, JGRA, 112, 6214

Roussos, E., Kollmann, P., Krupp, N., et al. 2018, Icar, 305, 160

Roussos, E., Kollmann, P., Krupp, N., et al. 2019, GeoRL, 46, 3590

Sauvaud, J. A., Walt, M., Delcourt, D., et al. 2013, JGRA, 118, 1723

Selesnick, R. S., Su, Y.-J., & Blake, J. B. 2016, JGRA, 121, 8417

Shprits, Y. Y., Menietti, J. D., Gu, X., Kim, K. C., & Horne, R. B. 2012, JGRA, 117, 11216

Su, Y.-J., Selesnick, R. S., & Blake, J. B. 2016, JGRA, 121, 8508

Summers, D., Ni, B., & Meredith, N. P. 2007, JGRA, 112, A04207

Sun, Y. X., Roussos, E., Krupp, N., et al. 2019, GeoRL, 46, 10240

Thomsen, M. F., Roussos, E., Andriopoulou, M., et al. 2012, JGRA, 117, A09208

Thomsen, M. F., & Van Allen, J. A. 1980, JGR, 85, 5831

Turner, D. L., O'Brien, T. P., Fennell, J. F., et al. 2017, JGRA, 122, 695

Ukhorskiy, A. Y., Sitnov, M. I., Mitchell, D. G., et al. 2014, Natur, 507, 338

Williams, P. K. G. 2018, in Handbook of Exoplanets, ed. H. J. Deeg & J. A. Belmonte (Cham: Springer), 171

Wilson, R. J., Bagenal, F., Delamere, P. A., et al. 2013, JGRA, 118, 2122

Wilson, R. J., Tokar, R. L., & Henderson, M. G. 2009, GeoRL, 36, 23104

Woodfield, E. E., Glauert, S. A., Menietti, J. D., et al. 2019, GeoRL, 46, 7191

Woodfield, E. E., Horne, R. B., Glauert, S. A., et al. 2018, NatCo, 9, 5062

Yamazaki, A., Tsuchiya, F., Sakanoi, T., et al. 2014, SSRv, 184, 259

Yoshikawa, I., Yoshioka, K., Murakami, G., et al. 2014, SSRv, 184, 237

Yoshioka, K., Murakami, G., Yamazaki, A., et al. 2013, P&SS, 85, 250

Yuan, C. J., Roussos, E., Wei, Y., & Krupp, N. 2020, JGRA, 125, e27621